PCCP

Accepted Manuscript

ROYAL SOCIETY OF CHEMISTRY

www.rsc.org/pccp

Journal Name

ARTICLE

X-ray Absorption Spectroscopy of Lithium Insertion and De-Insertion in Copper Birnessite Nanoparticle Electrodes†

Received 00th January 20xx,
Accepted 00th January 20xx

DOI: 10.1039/x0xx00000x

www.rsc.org/

Christopher J. Pelliccione,[a] Yue Ru Li,[b] Amy C. Marschilok,[b,c]* Kenneth J. Takeuchi[b,c]* and Esther S. Takeuchi[a,b,c]*

The combination of ex-situ X-ray diffraction (XRD) and X-ray absorption spectroscopy (XAS) measurements on 2D layered copper birnessite cathode materials for lithium ion battery applications provides detailed insight into both bulk-crystalline and localized atomic structural changes resulting from electrochemically driven lithium insertion and de-insertion. Copper birnessite electrodes that had been galvanostatically discharged and charged were measured with XRD to determine the accompanying long-range crystalline structure changes, while Mn and Cu K-edge XAS measurements provided a detailed view of the Mn and Cu oxidation state changes along with variations of the local neighboring atom environments around the Mn and Cu centers. While not detectable with XRD spectra, through XAS measurements it was determined that the copper ions (Cu^{2+}) are reduced to form amorphous nano-sized Cu metal, and can be oxidized back to Cu^{2+}. The reversible nature of the interconversion provides a rationale to the enhanced discharge capacity of copper birnessite relative to the analogous copper-free birnessite materials. The manganese oxide octahedra comprising the 2D layers in the original copper birnessite crystal structure disperse during lithium insertion, and revert back close to their original orientation after lithium de-insertion. During electrochemical oxidation or reduction the layered birnessite structure does not collapse, even though significant local disordering around Mn and Cu centers is directly observed.

Introduction

Manganese-based materials have received significant attention in the energy storage research literature in part due to their lower cost when compared to materials based on cobalt or nickel. Several types of manganese oxide materials including hollandite (2 x 2 tunnel, OMS-2),[1-5] and todorokite (3 x 3 tunnel, OMS-3)[6] have been investigated where quasi-reversible lithium ion electrochemistry is reported. The nature of the interlinking of MnO_6 octahedra within a structure create a variety of voids that can dramatically affect lithium-ion diffusion pathways. [1, 2, 7-9]

Birnessite is a layered manganese oxide with a monoclinic structure and a space group designation of C 2/m.[10, 11] Birnessite is comprised of layers of manganese-oxygen octahedra (MnO_6) with water molecules positioned between the MnO_6 layers. Although birnessite can be formed without any interlayer cations,[12, 13] monovalent (Na^+, K^+, Li^+, Cs^+)[14-16] or divalent (Mg^{2+} or Cu^{2+}) cations can also be incorporated between the layers through various synthesis techniques.[17-19] Typically, the interlayer cation is electrochemically inert; however, in the case of copper birnessite, there is an opportunity for the Cu^{2+} to be electrochemically active. Notably, there have been several reports on the electrochemical reactivity of copper ions in copper containing transition metal oxides, such as copper vanadium oxide.[20-26] In those reports, the formation of copper metal upon reduction was noted along with evidence of copper electrochemical reversibility. Therefore we hypothesized a similar electrochemical reversibility would be achievable for the copper birnessite material, where detailed x-ray absorption spectroscopy could lend insight into the discharge and charge process. To our knowledge, this is the first mechanistic exploration of the electrochemistry of copper birnessite.

Although birnessite-type cathodes can exhibit a high initial capacity (ca. 180 mAh/g or higher) significant capacity fade is often observed after multiple cycles.[27, 28] It has been postulated that in some birnessite cathodes manganese atoms migrate from the 2D layer of manganese oxide octahedra into the interlayer region and as a result reduce the cycle lifetime of the material.[29] Notably, some birnessite structures that incorporate cations, particularly divalent cations other than manganese, in the interlayer region have been reported to exhibit less capacity fade since the manganese migration process is inhibited.[16] The larger radii of the divalent cations within the interlayer region were asserted to provide structural support to the birnessite-type materials, resulting in prolonged cycle lifetimes.

[a] Brookhaven National Laboratory, Upton, NY 11973
[b] Department of Chemistry, Stony Brook University, Stony Brook, NY 11790
[c] Department of Materials Science and Engineering, Stony Brook University, Stony Brook, NY 11790
*corresponding authors: (ACM) amy.marschilok@stonybrook.edu, (KJT) kenneth.takeuchi.1@stonybrook.edu, (EST) esther.takeuchi@stonybrook.edu
†Electronic Supplementary Information (ESI) available: Full XAS fitting results. See DOI: 10.1039/x0xx00000x

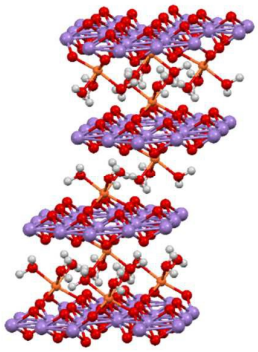

Fig. 1: Layered structure of copper birnessite ($Cu_xMnO_y \cdot nH_2O$) with Mn atoms in purple, Cu in orange, O in red and H in white

The copper birnessite structure, shown in **Figure 1**, includes copper ions along with water separating the manganese oxide 2D layers with an interlayer separation of ca. 7 Å.[7] The copper cations display tetrahedral coordination geometry using oxygen donor atoms, with a formal oxidation state of Cu^{2+}. Manganese is confined to the 2D layered structure as MnO_6 octahedra (Mn^{4+}), with a small fraction of Mn existing in Mn^{3+} oxidation state due to site vacancies.[18, 30] The copper birnessite material has the potential advantage over other divalent birnessite systems where copper may be electrochemically active and add to the total capacity of the electroactive material.

The study of energy storage materials after cycling often requires several techniques for characterization. For example, X-ray diffraction (XRD) techniques provide information on the crystalline phases of the material, but may not be suitable for characterization of structural changes in nanomaterials formed as a result of electrochemical reduction and oxidation, due to their small crystallite size and associated line broadening.[31-34] X-ray absorption spectroscopy (XAS), on the other hand, is particularly useful for characterizing the materials after electrochemical testing, as XAS can be used to accurately characterize both crystalline and highly disordered materials and is an element specific technique allowing only atoms of interest to be probed. XAS methods have been previously used to determine detailed electrochemical mechanisms which exhibited complex multi-step processes that involved primarily amorphous phases.[35-40] In general, XAS spectra contain two main regions, the X-ray absorption near edge structure (XANES) and the extended X-ray absorption fine structure (EXAFS) which are sensitive to the local electronic environment (i.e. oxidation state) and neighbouring atomic structure (coordination number, atomic identity and interatomic distance, etc.) respectively. The XANES region can be directly compared to standards of known oxidation states to determine the average oxidation state of the element of interest within the sample, while the EXAFS region can be analysed with theoretical structural models to extract details about the surrounding atomic environment within ca. 6 Å around the absorbing atom.

In this study, we utilize ex-situ XRD and XAS measurements to understand the lithium insertion and de-insertion of 2D layered structure of copper birnessite. XRD measurements were used to determine changes in the long-range crystallinity of the material. X-ray absorption near edge structure (XANES) was used to monitor the oxidation states of both Cu and Mn atoms. Modelling of the extended x-ray absorption fine structure (EXAFS) provided a detailed view of the local atomic structural changes occurring around Cu and Mn atoms within the electrode as a function of discharged or charged states. Further, in this first mechanistic study of the discharge-charge process for copper birnessite, we note partial reversibility of the Cu^{2+} reduction-Cu^0 oxidation process. Combining the results of these three techniques, we propose a lithium insertion and de-insertion mechanism that may be relevant to other birnessite-type cathodes.

Experimental Methods

The synthesis of copper birnessite ($Cu_xMnO_y \cdot nH_2O$) was adapted from a prior report,[41] and is presented here in brief. A modified redox coprecipitation and ion exchange method was used where manganese(II) nitrate tetrahydrate ($Mn(NO_3)_2 \cdot 4H_2O$), sodium hydroxide (NaOH) and sodium persulfate ($Na_2S_2O_8$) were used as starting materials.[42] The combination of these three precursors generated an isolated solid that was removed and added to an aqueous solution of cupric nitrate hemi(pentahydrate), ($Cu(NO_3)_2 \cdot 2.5H_2O$), yielding a final product of $Cu_xMnO_y \cdot nH_2O$. Thermogravimetric analysis/differential scanning calorimetry (TGA/DSC) along with inductively coupled plasma optical emission spectroscopy (ICP-OES) were used to accurately determine the ratio of Cu, Mn and H_2O present within the as synthesized samples as 12 nm $Cu_{0.27}MnO_{2.15} \cdot 1.03H_2O$ nanoparticles.

Electrochemical measurements were conducted in two electrode experimental coin cells consisting of lithium metal anode, $Cu_{0.27}MnO_2 \cdot 1.03H_2O$ cathode and a porous separator positioned between the electrodes. The cathodes contained copper birnessite as the active material, acetylene black carbon additive and polyvinylidene fluoride (PVDF) binder. The electrolyte used was 1.0 M $LiPF_6$ (or $LiBF_4$) in 1:1 ratio by volume of ethylene carbonate and dimethyl carbonate for all electrochemical testing. Each coin cell was galvanostatically cycled at 3.55×10^{-2} mA/cm^2 at a fixed temperature of 30°C within a voltage range of 3.8 and 2.0 V vs. lithium metal using a 6010AMaccor battery testing system. Copper birnessite electrodes used for ex situ XRD and XAS measurements were discharged to 2.0 V and charged to 3.8 V within a coin cell and removed at the specified state of discharge/charge. Scanning electron microscopy data was collected on a JEOL 6010A on samples mounted on double sided carbon tape (Figure S1). Samples for XAS measurements were sealed between polyimide tape to limit any oxidation from air exposure.

XRD measurements of pristine, discharged and charged electrodes were collected using a Rigaku MiniFlex600 X-ray powder diffractometer. Cu Kα radiation (λ= 0.1542 nm) was

used in a Bragg-Brentano focusing geometry. XRD spectra were measured between 5 to 90° in 2θ with 0.04° step size. The resulting XRD spectra were normalized through background subtraction and scaled such that the highest intensity peaks of each spectrum were consistent. Crystallite sizes of copper birnessite were estimated by using the Scherrer equation[43, 44] with the full width at half maximum (FWHM) of the (001) peak calculated using Peak Fit software after correcting for instrumental broadening using a LaB_6 standard.

Ex situ XAS measurements were taken at the Mn and Cu K-edges (6.539 and 8.979 keV respectively) on the X11A beamline at the National Synchrotron Light Source I at Brookhaven National Laboratory, NY using a double-crystal Si (111) crystal monochromator in transmission geometry with a reference foil measured simultaneously for accurate alignment of multiple XAS scans during analysis. A pristine starting state electrode was also measured for direct comparison of the structural changes observed in the cycled electrodes. Measurements of multiple standards of Mn and Cu oxidation states were also acquired for proper analysis of the XANES region.

All XAS data was aligned, merged, deglitched and normalized in Athena.[45, 46] The built-in AUTOBK algorithm was used to minimize background noise below R_{bkg} = 1.0 Å. The XANES region for both Cu and Mn K-edge spectra were analysed using linear combination fits (LCF) of standards with known oxidation states. For the Cu K-edge, metallic Cu and $Cu(NO_3)_2$ were used as standards for Cu^0 and Cu^{2+} oxidation states respectively. For the Mn K-edge, metallic Mn, Mn_3O_4, Mn_2O_3 and MnO_2 were all used as Mn^0, $Mn^{2+,3+}$, Mn^{3+} and Mn^{4+} oxidation state standards. The LCF were conducted in a range of 30 eV below to 50 eV above the absorption edge and all possible combinations of standard spectra were attempted during the fitting process to ensure the most accurate fit was achieved.

The Mn K-edge EXAFS spectra for each of the pristine, discharged to 2.0 V and charged to 3.8 V states were modelled using Artemis with theoretical models created by FEFF6.[47, 48] The pristine and charged spectra were fit using a modified zinc calcophanite crystal structure replacing Zn atoms with Cu.[49] The discharged spectrum was modelled based on a tetragonal Mn_3O_4 crystal structure in which Mn occupies two crystallographic sites with octahedral and tetragonal coordination to neighbouring oxygen atoms respectively.[50] All fits were conducted in a k-range of 2 – 10 $Å^{-1}$ in k and k^2 k-weightings simultaneously with dk = 2. The R-range was set to 1.0 – 2.9 Å for the pristine and charged spectra while the discharged data was fit in a range of 1.0 – 3.5 Å with a Hanning window to fully encompass both the first and second shell peaks. Full details of the fitting procedure and results are discussed in the Electronic Supplementary Information.

The Cu K-edge EXAFS spectra fits were limited to only the first shell due to poor signal to noise ratio. The first shell, which consists of Cu-O contributions, was fit with a single Cu-O path using a quick-fit FEFF calculation. The corresponding amplitude and interatomic distance of this single Cu-O path was determined. The fits were conducted in a k-range of 2 – 9 $Å^{-1}$ in k and k^2 k-weightings simultaneously. The R-range was set to 1.0 – 2.0 Å using a Hanning window to fit only the first shell peak.

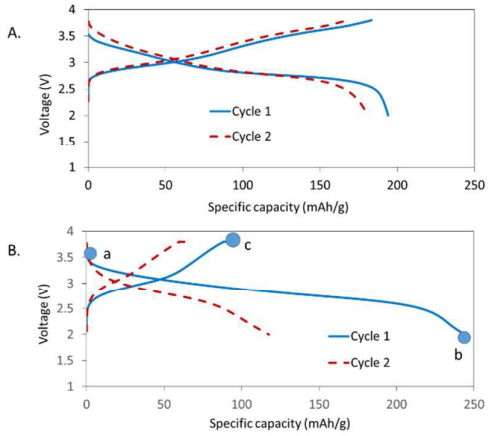

Fig. 2: First and second cycle discharge and charge curves of lithium/copper birnessite cells. A. using $LiPF_6$ electrolyte and B. using $LiBF_4$ electrolyte. Blue circles indicate the samples for XAS measurement: (a) pristine, (b) discharged to 2.0 V and (c) recharged to 3.8 V. Samples for XAS were collected from different coin cells.

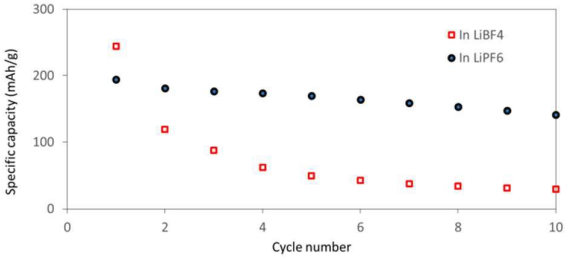

Fig. 3: Discharge and charge cycling of lithium/copper birnessite cells using $LiPF_6$ electrolyte or $LiBF_4$ electrolyte.

Results and Discussion

Electrochemical Testing. **Figure 2** shows the first and second discharge and charge curves of lithium/copper birnessite cells using two different electrolyte systems, $LiPF_6$ and $LiBF_4$. Both electrolytes show the presence of two plateaus on discharge and charge. In $LiPF_6$ electrolyte, there was a small amount of capacity loss between cycles one and two, **Figure 2A**. Notably, the samples in $LiBF_4$ electrolyte showed significant irreversible capacity as the first discharge delivered ~250

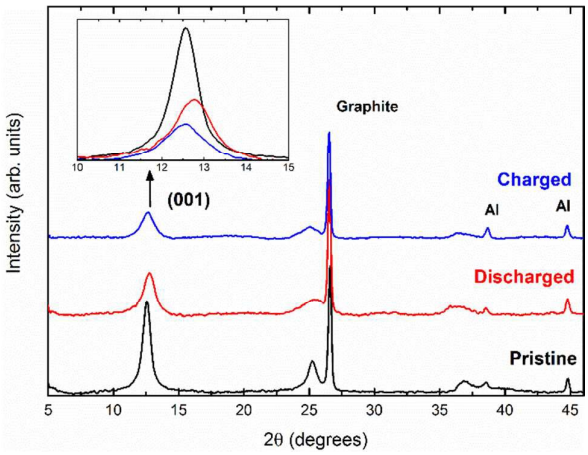

Fig. 4: XRD spectra of pristine, discharged and charged copper birnessite. The peak at ca. 26° in 2θ is from the carbon additive and other peaks at ca. 38° and 44° are from the Al substrate. The inset displays a detailed overlay of the (001) reflection.

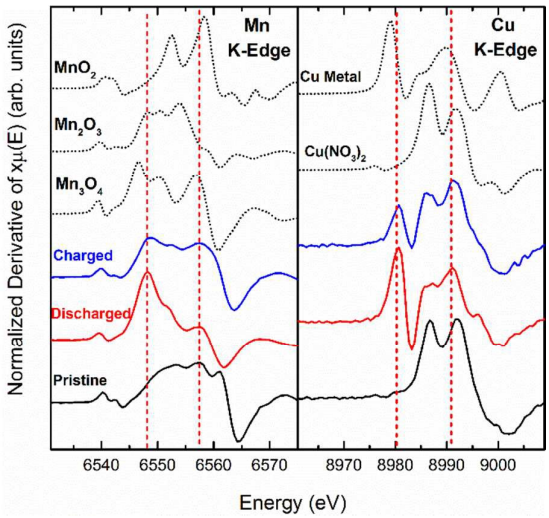

Fig. 5: First derivative of xμ(E) for pristine, discharged to 2.0 V (red) and charged to 3.8 V (blue) electrodes at both Mn and Cu K-edges with corresponding standards (dotted black lines). Vertical red dashed lines indicate prominent features in the discharged spectrum.

mAh/g (or ca. 1.1 e^- equivalents per manganese center) while the first charge provided only 100 mAh/g, **Figure 2B.** Additional cells were utilized where they were discharged and charged for 10 cycles, **Figure 3.** While the initial capacity is higher for the cells using the $LiBF_4$ electrolyte, the decrease in capacity with additional cycles is notable. The cells using $LiPF_6$ electrolyte show an initial capacity ~200 mAh/g and show much improved capacity retention where the capacity at cycle 8 is ~ 159 mAh/g.

A prior report presented electrochemical evaluation of sodium birnessite, $Na_{0.35}MnO_2{\cdot}H_2O$, in lithium anode batteries using $LiPF_6$ based electrolyte. Galvanostatic discharge-charge curves were measured with a voltage window between 4.2 and 2.0 V. The initial cycle of $Na_{0.35}MnO_2{\cdot}H_2O$ delivered ~140 mAh/g and ~85 mAh/g after 8 cycles (~40% capacity fade).[10] The lithium/copper birnessite cell with 1M $LiPF_6$ based electrolyte delivered about 200 mAh/g initial capacity and after 8 cycles, delivered ~160 mAh/g capacity (~20% capacity fade). Thus, the copper birnessite showed enhanced capacity retention over previously reported results for sodium birnessite.

Analysis of discharged and charged **$Cu_{0.27}MnO_2{\cdot}1.03H_2O$.** Samples from the cells shown in **Figure 2B** were selected for the XAS measurements to gain insight into materials associated with the significant capacity loss between the first and second cycle. X-ray powder diffraction, XANES, and EXAFS analysis were used for the study.

X-ray diffraction**. Fig. Figure 4** shows the ex situ XRD spectra for the pristine, discharged and charged copper birnessite electrodes. The most prominent peak from each spectrum is from the (001) plane located at ca. 12.5° in 2θ which corresponds to the c-axis separation between manganese oxide layers. This interlayer separation of ca. 7.1 Å corresponds well to the comparable magnesium birnessite crystal structure.[17] When the electrode is discharged to 2.0 V, this (001) peak broadens and loses intensity, indicating smaller crystallite sizes (estimated as ca. 9 nm via the Scherrer equation) and possible amorphization of the material. There is also a slight shift of the (001) peak to ca. 12.8° in 2θ, indicating a slight compression of the interlayer separation to ca. 6.9 Å. When the electrode is recharged, there are subtle variations in the (001) peak with respect to the FWHM and intensity indicating minor crystallite size and overall crystallinity changes. However, the Bragg reflection shifts back to ca. 12.5°, indicating the interlayer spacing returns to ca. 7.1 Å.

Although there are structural changes occurring during lithium insertion and de-insertion, it is clear that the general crystal structure of the pristine material remains after one cycle- i.e. the layered 2D structure does not fully collapse after lithium insertion. In addition, when the material is discharged, there is no evidence of any other phases such as manganese oxides or other copper based phases, particularly copper metal with expected diffraction peak at ca. 43°.[51] This may be due to the amorphous nature of the created phases or, if crystalline, the small crystallite sizes does not produce sufficient periodic scattering to be observed in the XRD spectrum.

XANES. The XANES region of each XAS spectrum was directly compared to standards with varying oxidation states as shown in **Figure 5**. In the Mn K-edge data, through LCF results (**Table 1**), the pristine material was determined to be a combination of Mn^{3+} and Mn^{4+} oxidation states, as expected.[18] When discharged to 2.0 V, the edge position shifts to lower energy, suggesting on average Mn atoms are being reduced to lower

Table 1: Linear combination fit results for XANES of pristine, discharged to 2.0 V and charged to 3.8 V spectra for both Mn and Cu K-edges.

	R-factor (%)	$\%Mn_3O_4$	$\%Mn_2O_3$	$\%MnO_2$	R-factor (%)	$\%Cu(NO_3)_2$	%Cu
Pristine	0.37	0	25 ± 2	75 ± 3	1.10	100	0
Discharged	0.31	100	0	0	0.68	34 ± 4	63 ± 3
Charged	0.10	60 ± 1% Pristine, 40 ± 1% Mn_3O_4			0.48	81 ± 3	20 ± 3

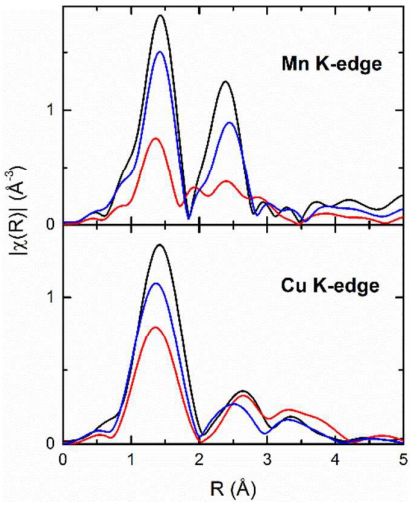

Fig. 6: |χ(R)| of the pristine (black), discharged (red) and charged (blue) for both Mn and Cu K-edges. Fourier transforms were performed using a k-range of 2 – 10 $Å^{-1}$ in k^2 k-weighting.

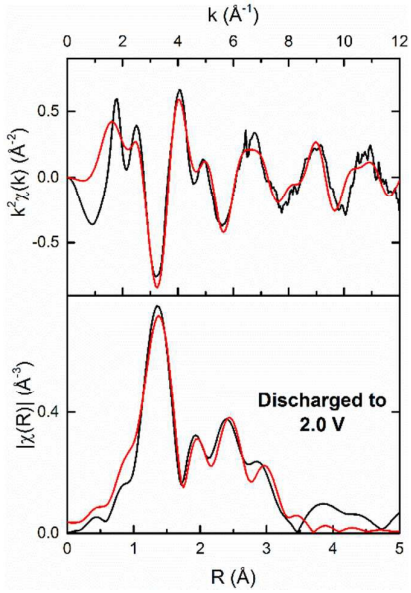

Fig. 7: Data (black) and corresponding fit (red) of the discharged to 2.0 V state in $k^2\chi(k)$ and |χ(R)|

oxidation states. LCF of the spectrum indicate Mn is entirely in a Mn_3O_4-like $Mn^{2+,3+}$ oxidation state. However, visually the discharged spectrum only slightly resembles the Mn_3O_4 XANES curve (**Figure 5**). This discrepancy can be explained through distortion in the local coordination environment around Mn atoms compared to the standard Mn_3O_4 crystal structure. Shifts in the interatomic distance to close neighboring atoms, and even a slight alteration in the coordination geometry can result in variations in the XANES region regardless of formal oxidation state changes.[52-54] When the electrode is recharged, Mn partially reverts back to the oxidation state of the pristine birnessite-type structure, with 40 ± 1% of the Mn atoms remaining in the discharged $Mn^{2+,3+}$ oxidation state.

The Cu atoms exhibit a more straightforward XANES transition. All Cu atoms are initially in Cu^{2+} oxidation state as dictated from the initial crystal structure and confirmed through LCF analysis. Upon electrochemical discharge and lithiation of the copper birnessite, 63 ± 3% of Cu reduces to metallic Cu, while the rest remains as Cu^{2+}. Upon charge and delithiation, the conversion is mostly reversible, with only 20 ± 3% of the Cu remaining in a metallic state. Visually, the XANES region of each electrode state is comparable to the standards of Cu metal and $Cu(NO_3)_2$ with respect to peak positions and relative intensities (**Figure 4**). This suggests a direct conversion to and from each oxidation state, with minor distortion of the neighboring atomic environment as observed in the Mn K-edge XANES.

***EXAFS*. Mn K-edge**: |χ(R)| (Fourier transform of χ (k)) of both the Mn and Cu K-edges are shown in **Figure 6**. The interatomic distances displayed in **Figure 6** are not corrected for phase shifts, so peaks will be represented at shorter distances than fitting results indicate. In the pristine electrode, EXAFS modeling determined that Mn has two distinct Mn-O interatomic distances of 1.87 ± 0.01 and 1.94 ± 0.01 Å in a 2:1 ratio of the number of oxygen atoms at each distance respectively. This result is consistent with the expected 2D layers of MnO_6 octahedra in the birnessite structure.[55] There are two Mn-Mn distances of 2.81 ± 0.01 Å and 2.92 ± 0.01 Å that create the second shell peak located between 2.0 – 3.0 Å in **Figure 4** and are also in agreement with the expected birnessite-type crystal structure.

When the electrode is discharged, significant changes in the Mn K-edge |χ(R)| spectrum are observed (**Figure 6**). A decrease in the number of neighboring oxygen atoms is detected from the reduction in intensity of the first shell peak at ca. 1.5 Å, along with considerable reorganization of the second shell between 2.0 – 3.0 Å as indicated by the three distinct peaks (ca. 2.0, 2.5 and 2.9 Å) in contrast from the

Table 2: EXAFS fitting results for the discharged state along with calculated amplitude and distance for the standard Mn_3O_4 crystal structure.

	Mn_3O_4 Structure				Modeling Results	
	Octahedral Site		Tetrahedral Site			
	Near Neighbors	Distance (Å)	Near Neighbors	Distance (Å)	Near Neighbors	Distance (Å)
Mn-O	2.7	1.93	1.3	2.04	2.3 ± 0.4	1.92 ± 0.01
	1.3	2.28	2.7		1.1 ± 0.3	2.18 ± 0.01
	1.3	3.55			1.1 ± 0.8	3.47 ± 0.03
					3.4 ± 0.8	3.56 ± 0.03
Mn-Mn	1.3	2.88	2.7	3.48	1.0 ± 0.4	2.96 ± 0.03
	2.7	3.12				
	2.7	3.43				

initial single peak (ca. 2.4 Å) in the pristine state. This type of reorganization of the second shell has been observed in similar manganese oxide XAS studies in Mg^{2+} battery chemistries.[56] Using the information obtained from the XANES analysis, this discharged spectrum was fit using a model based on the Mn_3O_4 structure that consists of two crystallographic sites for Mn atoms, one in which Mn has octahedral coordination to oxygen and the other tetrahedral coordination with Mn atoms occupying each site in a 2:1 ratio respectively. It is also expected from the XANES that the structure is highly distorted, so the fitting model accounted for this by allowing many of the Mn-O distances and amplitudes to vary independently from the standard Mn_3O_4 crystal structure. The resulting model closely mimics the experimental data, as shown in **Figure 7** with the detailed results presented in **Table 2**. The fit results in nearest Mn-O distances of 1.92 ± 0.01 and 2.18 ± 0.01 Å. In the standard Mn_3O_4 structure, the Mn atoms in octahedral sites have neighboring oxygen atoms located at 1.93 Å and 2.28 Å while the tetrahedrally coordinated sites have oxygen atoms located at 2.04 Å. With the number of oxygen atoms again in a 2:1 ratio for the shortest two interatomic distances, and without direct observation of the 2.04 Å distance prescribed to tetrahedrally coordinated Mn, this model suggests the majority of Mn remain in octahedral coordination to neighboring oxygen atoms.

The number of near neighbors of all Mn-O and Mn-Mn paths are lower than expected for the standard Mn_3O_4 structure (**Table 2**). This is likely due to the considerable disorder and the nano-scale of the system reducing the average number of neighboring O and Mn atoms seen by each Mn atom.[57, 58] The disorder in the discharged state is evident when comparing the Mn-Mn modeling results to the starting birnessite or standard Mn_3O_4 crystal structures. The model consists of only one Mn-Mn distance at 2.96 ± 0.03 Å, and a bulk Mn_3O_4 environment would have three distinct Mn-Mn distances of 2.88, 3.12 and 3.43 Å due to the Mn atoms in octahedral sites, while the birnessite structure has Mn-Mn distances of 2.81 ± 0.01 and 2.92 ± 0.01 Å. The observed Mn-Mn interatomic distance suggest that clusters of two or three MnO_6 octahedra are somewhat isolated from neighboring octahedra clusters, accounting for the significantly reduced number of neighboring manganese atoms and total number of distinct Mn-Mn distances. This type of segregation of MnO_x has been suggested through density functional theory (DFT) calculations of the lithiation process of similar MnO_2 based materials.[59, 60]

When the material is recharged, the Mn atoms return to a similar configuration as the pristine sample, with oxygen atoms located at 1.88 ± 0.02 and 1.94 ± 0.02 Å, which are within estimated standard deviation of the original structure (1.87 ± 0.01 and 1.94 ± 0.01 Å in the pristine state) along with identical number of oxygen atoms at each Mn-O distance. There is however ca. 40% reduction in number of neighboring Mn atoms observed in the second shell. This is likely due to the disorder observed in the discharged spectrum prohibiting full conversion back to the original 2D MnO_6 layers. However, the observation of a local environment that is similar to the pristine sample suggests that the layered architecture of the original crystal structure is not broken when discharged, and the relative disorder observed around Mn atoms occurs within the confines of these 2D planes. This result from EXAFS analysis is in agreement with XRD analysis (**Figure 3**).

To complement the EXAFS theoretical modeling results, a continuous Cauchy wavelet transform (CCWT) was applied to each spectrum to help identify the atomic species that form the peaks observed in **Figure 6**. The wavelet transform allows the EXAFS spectrum to be viewed in three dimensions: the wavenumber, k, the interatomic distance from the absorbing atom (uncorrected for phase shifts), R, and the modulus of the wavelet transform. The CCWT provides additional insight not clear from basic Fourier transform analysis as low-Z elements tend to scatter more effectively at lower k-values, while high-Z elements scatter at larger k-values, this technique provides some degree of resolution to differentiate atomic species present throughout the EXAFS spectrum.[61-63] This technique has proven to be quite valuable when trying to differentiate elements that are located at similar interatomic distances and thus their contributions become convoluted into a single broad peak in R-space using traditional Fourier transforms.[64, 65] In this study, this technique was utilized to confirm the structural changes observed from EXAFS modeling results, particularly in the discharged state to support the observation of isolated manganese oxide clusters.

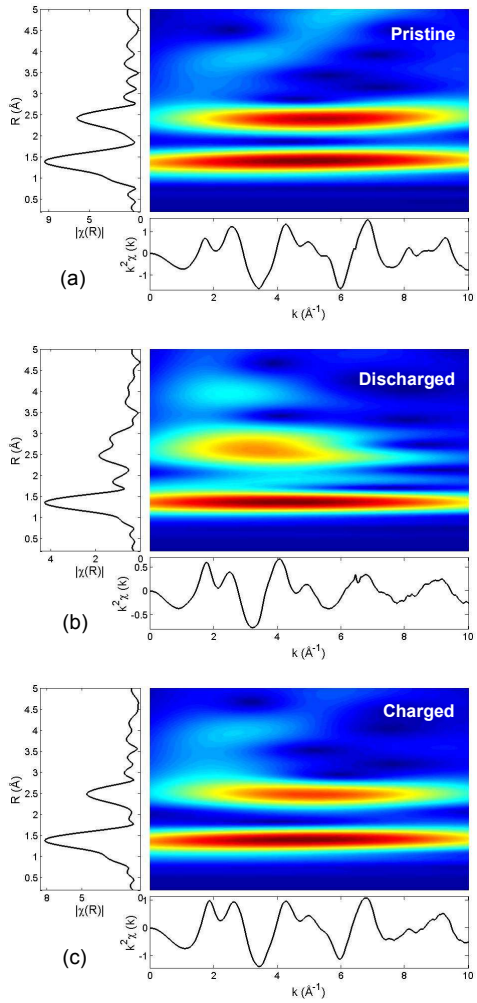

Fig. 8: Continuous wavelet analysis of (a) pristine, (b) discharged and (c) charged EXAFS spectrum.

Figure 8 shows the pristine, discharged and charged Mn K-edge wavelet modulus spectra generated from a script provided by Muñoz *et al.*[61] In the pristine state (**Figure 8a**), the heat-map displays two clear peaks centered in R-space at ca. 1.4 and 2.5 Å. These two peaks are slightly offset in the heat-map in the k-dimension (ca. 4.5 and 5.5 $Å^{-1}$ respectively) suggesting that these peaks are different element species, oxygen and manganese specifically. When the material is discharged (**Figure 8b**), the peak in the heat-map centered at ca. 2.5 Å shifts to a much lower k-value of ca. 3.5 $Å^{-1}$. This dramatic shift away from the original position of ca. 5.5 $Å^{-1}$ indicates this very broad second shell in R-space is primarily comprised of low-Z elements (i.e. oxygen) with little contribution from the higher-Z Mn atoms. This observation is in agreement with the EXAFS modeling results, suggesting that the dramatic decrease in the number of neighboring Mn atoms requires the manganese oxide octahedra to be fairly well isolated from one another. When the material is recharged, the heat-map looks remarkably similar to the pristine state

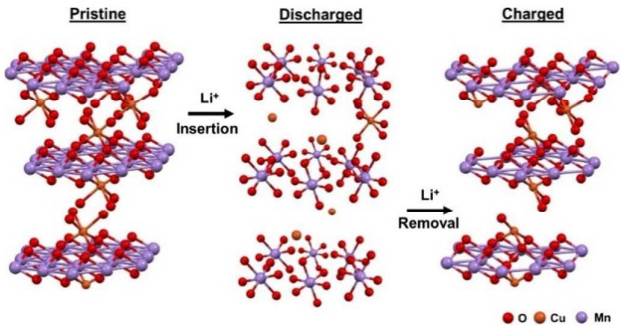

Fig. 9: Schematic of the proposed discharge/charge process of copper birnessite. Li/Li_2O and H_2O not pictured for simplicity

(**Figure 8a**), suggesting Mn returns close to the original layered structure as observed in the EXAFS modeling and XRD results.

Cu K-edge: CuO is fairly isolated in the original layered structure with the nearest Mn atom ca. 3.5 Å away, and as a consequence the only significant contribution to the EXAFS signal is from Cu-O, which was modeled as a single Cu-O interatomic distance.[66] As expected from the XANES analysis, the number of oxygen neighbors decreases from the tetrahedral-like 3.9 ± 0.8 oxygen atoms in the pristine structure to 1.8 ± 0.7 oxygen atoms in the discharged structure. There is also a noticeable shift in Cu-O distance from 1.95 ± 0.02 Å to 1.85 ± 0.03 Å in the pristine and discharged states respectively. When recharged, the number of oxygen atoms increases to 2.9 ± 0.7 at a distance of 1.90 ± 0.02 Å. As was observed at the Mn K-edge, when the material is recharged Cu does not completely revert back to the pristine structure, but there is clearly some degree of reversibility of copper oxidation.

Qualitatively, although there are large shifts in the Cu-O environment, the second shell peak between ca. 2.5 - 3.0 Å does not show significant changes in either peak height or position (**Figure 6**). From the XANES analysis, it was identified that ca. 60% of Cu atoms convert to a metallic oxidation state. With no direct observation of Cu metal peaks (observed at ca. 2.2 Å in R-space for cubic Cu metal[51]) it implies that Cu atoms are well dispersed and isolated within the crystal structure preventing the Cu atoms from combining into larger metallic particles. This isolation of Cu atoms likely aides the reversible oxidation observed in both XANES and EXAFS results.

Lithiation Insertion and De-insertion Mechanism

Ex situ XRD and XAS analysis has facilitated a detailed characterization of the long-range and local structural changes occurring around both Mn and Cu atoms of copper birnessite after being discharged to 2.0 V and recharged to 3.8 V. **Figure 9** summarizes results derived from XANES and EXAFS modeling that indicate the lithium ions reversibly convert oxygen to Li_2O, particularly near Cu atoms located between manganese oxide

2D layers, as a clear reduction in oxidation state of ca. 65% of Cu atoms from Cu^{2+} to Cu^0 is observed. When lithium atoms are removed, ca. 80% of copper atoms return to a Cu^{2+} oxidation state with ~20% remaining in the metallic state. This trend was confirmed in the Cu K-edge EXAFS modeling results of the first shell peak with the number of neighboring oxygen atoms decreasing from ca. 4 oxygen atoms to ca. 2 atoms in the discharged state, and then restoring close to the original value with ca. 3 oxygen atoms when recharged. The response of the copper center under lithium insertion and subsequent lithium deinsertion is illustrated in the equations below.

Li insertion: $Cu^{2+} + 1.3e^- \rightarrow 0.65Cu^0 + 0.35Cu^{2+}$

Li deinsertion: $0.65(Cu^0 \rightarrow 0.2Cu^0 + 0.8Cu^{2+} + 1.6e^-)$

Thus, based on the XAS, we estimate that ~80% of the copper metal formed upon discharge is oxidized during the charge step, suggesting the copper reduction is largely reversible. Thus, the significant capacity loss from the first cycle in $LiBF_4$ electrolyte is due to irreversibility at both the Mn and Cu centers.

The 2D MnO_6 layers of copper birnessite undergo significant structural changes during lithium insertion and de-insertion. The XANES LCF and EXAFS modeling results indicate that when lithium is incorporated into the structure, the original birnessite-type manganese oxide octahedra become highly disordered and transform into Mn_3O_4-like octahedra with an observed expansion of Mn-O interatomic distances compared to the starting state birnessite structure (ca. 3-5% oxygen interatomic distance expansion). The single observed Mn-Mn distance (2.96 ± 0.03 Å) and particularly the small number of neighboring Mn atoms (1.0 ± 0.4) suggest that two or three Mn_3O_4-like manganese oxide octahedra cluster together while predominantly isolating themselves from neighboring clusters. It is anticipated that Li/Li_2O fill the voids between manganese oxide clusters, as suggested from density functional theory calculations of similar MnO_2 electrodes.[59, 60] All of these transformations around Mn atoms must occur within the confines of the original 2D planes, as the XRD spectra show a retention of the original layered birnessite structure (**Figure 4**). If the layered architecture were to collapse during lithium insertion or de-insertion, the Bragg reflection from the periodic structure along the c axis (001) plane would disappear, and in all electrochemical states this (001) peak is prominent in the XRD measurements.

When the electrode is recharged to 3.8 V, the manganese atoms revert to a structure analogous to the starting state birnessite as evidenced from the Mn-O distances returning within estimated standard deviations to the original values and the relative ratio of oxygen atoms between these paths corresponding to the pristine structure. In addition, as was discussed previously, the XRD spectra for the charged state is not appreciably different from the pristine state outside of a slight broadening of the (001) peak. However, from the EXAFS spectrum the number of neighboring manganese atoms in the second shell are considerably reduced compared to the original structure. This indicates that the material does not entirely return to the starting state. It is conceivable that the extreme disorder observed in the discharged state limits the ease in which the reduced manganese can return to the original birnessite structure. However, even though there is reorganization of the local structure, the general architecture of alternating 2D layers of MnO_6 octahedra and CuO appears to remain intact as the local structure of manganese displays interconversion along with minor fluctuations of the long-range periodic structure, **Figure 9**.

Conclusions

Analysis of both ex situ XRD measurements along with XANES and EXAFS spectra of discharged and charged states of copper birnessite provides unique insight into the complex structural shifts that occur during lithium insertion and de-insertion. The long-range periodic structure of the material is not significantly affected from cycling as indicated by the minor changes observed in the XRD spectra. The XAS measurements however elucidate the complex rearrangement of the local structure around both Cu and Mn atoms when in a discharged state. Cu atoms interconvert between Cu^{2+} and Cu^0, adding to the observed capacity of this birnessite material. In addition, the manganese octahedra that are located in 2D layers in the crystal structure are converted to well dispersed Mn_3O_4-like octahedra confined to the original 2D architecture of the crystal structure. The large structural alterations observed in the discharged state are primarily reversible, as the charged state is remarkably similar to the pristine state around both Cu and Mn centers, indicating that the layered structure does not collapse during lithium insertion or de-insertion. However, significant capacity loss is noted during the first discharge and charge cycle and is attributed to some irreversibility at both the copper and manganese centers.

Acknowledgements

This work was supported as part of the Center for Mesoscale Transport Properties, an Energy Frontier Research Center supported by the U.S. Department of Energy, Office of Science, Basic Energy Sciences, under award #DE-SC0012673. X-ray absorption spectra were collected on X11A beamline at the National Synchrotron Light Source (NSLS-I) at Brookhaven National Laboratory supported by the DOE, Office of Science, BES, under Contract No. DE-AC02-98CH10886. Authors acknowledge K. Pandya for assistance with collection of XAS spectra.

References

1. K. J. Takeuchi, S. Z. Yau, M. C. Menard, A. C. Marschilok and E. S. Takeuchi, *ACS Applied Materials & Interfaces*, 2012, **4**, 5547-5554.
2. S. Zhu, A. C. Marschilok, E. S. Takeuchi and K. J. Takeuchi, *Electrochemical and Solid-State Letters*, 2009, **12**, A91-A94.

3. K. J. Takeuchi, S. Z. Yau, A. Subramanian, A. C. Marshilok and E. S. Takeuchi, *Journal of The Electrochemical Society* 2013, **160**, A3090-A3094.
4. L. Wu, F. Xu, Y. Zhu, A. B. Brady, J. Huang, J. L. Durham, E. Dooryhee, A. C. Marschilok, E. S. Takeuchi and K. J. Takeuchi, *ACS Nano*, 2015, **9**, 8430–8439.
5. S. Zhu, A. C. Marschilok, C.-Y. Lee, E. S. Takeuchi and K. J. Takeuchi, *Electrochemical and Solid-State Letters*, 2010, **13**, A98-A100.
6. N. Kumagai, S. Komaba, H. Sakai and N. Kumagai, *Journal of Power Sources*, 2001, **97–98**, 515-517.
7. S. Devaraj and N. Munichandraiah, *The Journal of Physical Chemistry C*, 2008, **112**, 4406-4417.
8. Z. Sun, H. Chen, D. Shu, C. He, S. Tang and J. Zhang, *Journal of Power Sources*, 2012, **203**, 233-242.
9. C. Wei, L. Deyao, Y. Jinkua, Y. Yong and L. Zugeng, *Journal of Electrochemistry*, 1999, **5**, 74-79.
10. M. Nakayama, T. Kanaya, J.-W. Lee and B. N. Popov, *Journal of Power Sources*, 2008, **179**, 361-366.
11. J. E. Post and D. R. Veblen, *American Mineralogist*, 1990, **75**, 477-489.
12. S. Bach, J. P. Pereira-Ramos, N. Baffier and R. Messina, *Electrochimica Acta*, 1991, **36**, 1595-1603.
13. S. Bach, J. P. Pereira-Ramos and N. Baffier, *Journal of Solid State Chemistry*, 1995, **120**, 70-73.
14. H. Kanoh, W. Tang, Y. Makita and K. Ooi, *Langmuir*, 1997, **13**, 6845-6849.
15. E. Silvester, A. Manceau and V. A. Drits, *American Mineralogist*, 1997, **82**, 962-978.
16. M. Tsuda, H. Arai and Y. Sakurai, *Journal of Power Sources*, 2002, **110**, 52-56.
17. B. J. Aronson, A. K. Kinser, S. Passerini, W. H. Smyrl and A. Stein, *Chem. Mater.*, 1999, **11**, 949-957.
18. C. Julien, M. Massot, R. Baddour-Hadjean, S. Franger, S. Bach and J. P. Pereira-Ramos, *Solid State Ionics*, 2003, **159**, 345-356.
19. A. Ogata, S. Komaba, R. Baddour-Hadjean, J. P. Pereira-Ramos and N. Kumagai, *Electrochimica Acta*, 2008, **53**, 3084-3093.
20. M. Morcrette, P. Rozier, L. Dupont, E. Mugnier, L. Sannier, J. Galy and J. M. Tarascon, *Nat. Mater.*, 2003, **2**, 755-761.
21. Y. Sakurai, H. Ohtsuka and J. Yamaki, *Journal of the Electrochemical Society*, 1988, **135**, 32-36.
22. H. Ma, S. Zhang, W. Ji, Z. Tao and J. Chen, *J. Am. Chem. Soc.*, 2008, **130**, 5361-5367.
23. M. Eguchi, T. Iwamoto, T. Miura and T. Kishi, *Solid State Ionics*, 1996, **89**, 109-116.
24. J.-q. Cao, X.-y. Wang, A. Tang, X. Wang, Y. Wang and W. Wu, *J. Alloys Compd.*, 2009, **479**, 875-878.
25. X. Cao, J. Xie, H. Zhan and Y. Zhou, *Materials Chemistry and Physics*, 2006, **98**, 71-75.
26. Y. Wei, C. W. Ryu, G. Chen and K. B. Kim, *Electrochem. Solid-State Lett.*, 2006, **9**, A487-A489.
27. S. Bach, J.-P. Pereira-Ramos, C. Cachet, M. Bode and L. T. Yu, *Electrochimica Acta*, 1995, **40**, 785-789.
28. R. Chen and M. S. Whittingham, *Journal of The Electrochemical Society*, 1997, **144**, L64-L67.
29. C. Rongji and M. S. Whittingham, *J. Electrochem. Soc*, 1997 **144(4):** , L64-L67.
30. J. Peña, J. R. Bargar and G. Sposito, *Chemical Geology*, 2015, **396**, 196-207.
31. A. S. Andersson, B. Kalska, L. Häggström and J. O. Thomas, *Solid State Ionics*, 2000, **130**, 41-52.
32. J. Chouvin, C. Branci, J. Sarradin, J. Oliver-Fourcade, J. C. Jumas, B. Simon and P. Biensan, *J. Power Sources*, 1999, **81-82**, 277-281.
33. P. Poizot, S. Laruelle, S. Grugeon, L. Dupont and J. M. Tarascon, *Nature*, 2000, **407**, 496-499.
34. J. Vetter, P. Novák, M. R. Wagner, C. Veit, K. C. Möller, J. O. Besenhard, M. Winter, M. Wohlfahrt-Mehrens, C. Vogler and A. Hammouche, *Journal of Power Sources*, 2005, **147**, 269-281.
35. M. Balasubramanian, X. Sun, X. Q. Yang and J. McBreen, *Journal of Power Sources*, 2001, **92**, 1-8.
36. C. J. Pelliccione, Y. Ding, E. V. Timofeeva and C. U. Segre, *Journal of The Electrochemical Society*, 2015, **162**, A1935-A1939.
37. C. J. Pelliccione, E. V. Timofeeva, J. P. Katsoudas and C. U. Segre, *J. Phys. Chem. C*, 2013, **117**, 18904-18912.
38. C. J. Pelliccione, E. V. Timofeeva and C. U. Segre, *Chem. Mater.*, 2015, **27**, 574-580.
39. Y. Shiraishi, I. Nakai, T. Tsubata, T. Himeda and F. Nishikawa, *Journal of Solid State Chemistry*, 1997, **133**, 587-590.
40. H. Yamaguchi, A. Yamada and H. Uwe, *Physical Review B*, 1998, **58**, 8-11.
41. R. Giovanoli, E. Stahli and W. Feitknrcht, *Helvetica Chimica Acta*, 1970, **53**, 209-220.
42. Y. R. Li, A. C. Marschilok, E. S. Takeuchi and K. J. Takeuchi, *Journal of the Electrochemical Society*, 2016, **163**, A1-A5.
43. A. Patterson, *Phys. Rev.*, 1939, **56**, 978-982.
44. P. Scherrer, N. Ges and w. Goettingen, *Math.-Phys. Kl*, 1918, **96**.
45. M. J. Newville, *J. Synchrotron Radiat.*, 2001, **8**, 322-324.
46. B. Ravel and M. Newville, *Journal of Synchrotron Radiation*, 2005, **12**, 537-541.
47. J. Mustre de Leon, J. J. Rehr, S. I. Zabinsky and R. C. Albers, *Phys. Rev.*, 1991, **B44**, 4146.
48. J. Rehr, J. M. de Leon, S. Zabinsky and R. C. Alberts, *J. Am. Chem. Soc.*, 1991, **113**, 5135-5135.
49. J. E. Post and D. E. Appleman, *American Mineralogist*, 1988, **73**, 1401.
50. D. Jarosch, *Mineral and Petrology*, 1987, **37**, 15-23.
51. H. M. Otte, *J. Appl. Phys.*, 1961, **32**, 1536-1546.
52. H. Visser, E. Anxolabéhère-Mallart, U. Bergmann, P. Glatzel, J. H. Robblee, S. P. Cramer, J.-J. Girerd, K. Sauer, M. P. Klein and V. K. Yachandra, *Journal of the American Chemical Society*, 2001, **123**, 7031-7039.
53. G. A. Waychunas, *American Mineralogist*, 1987, **72**, 89-101.
54. M. Wilke, F. Farges, P.-E. Petit, G. E. Brown Jr and F. Martin, *American Mineralogist*, 2001, **86**, 714-730.
55. A. Manceau, A. I. Gorshkov and V. A. Drits, *American Mineralogist*, 1992, **77**, 1144-1157.
56. R. Zhang, X. Yu, K.-W. Nam, C. Ling, T. S. Arthur, W. Song, A. M. Knapp, S. N. Ehrlich, X.-Q. Yang and M. Matsui, *Electrochemistry Communications*, 2012, **23**, 110-113.
57. A. M. Beale and B. M. Weckhuysen, *Physical Chemistry Chemical Physics*, 2010, **12**, 5562-5574.
58. V. V. Srabionyan, A. L. Bugaev, V. V. Pryadchenko, L. A. Avakyan, J. A. van Bokhoven and L. A. Bugaev, *Journal of Physics and Chemistry of Solids*, 2014, **75**, 470-476.

59. D. A. Tompsett, S. C. Parker, P. G. Bruce and M. S. Islam, *Chemistry of Materials*, 2013, **25**, 536-541.
60. D. A. Tompsett and M. S. Islam, *Chemistry of Materials*, 2013, **25**, 2515-2526.
61. M. Munoz, P. Argoul and F. Farges, *American Mineralogist* 2003, **88**, 694-700.
62. H. Funke, A. C. Scheinost and M. Chukalina, *Physical Review B*, 2005, **71**, 094110.
63. J. Timoshenko and A. Kuzmin, *Computer Physics Communications*, 2009, **180**, 920-925.
64. E. H. Otal, E. Sileo, M. H. Aguirre, I. O. Fabregas and M. Kim, *Journal of Alloys and Compounds*, 2015, **622**, 115-120.
65. M. Filez, E. A. Redekop, H. Poelman, V. V. Galvita and G. B. Marin, *Analytical Chemistry*, 2015, **87**, 3520-3526.
66. J. Peña, J. R. Bargar and G. Sposito, *Chemical Geology*, 2015, **396**, 196-207.